

Point Cloud Change Detection With Stereo V-SLAM: Dataset, Metrics and Baseline

Zihan Lin¹, Jincheng Yu¹, Lipu Zhou², Xudong Zhang¹, Jian Wang¹, Yu Wang¹

Abstract—Localization and navigation are basic robotic tasks requiring an accurate and up-to-date map to finish these tasks, with crowdsourced data to detect map changes posing an appealing solution. Collecting and processing crowdsourced data requires low-cost sensors and algorithms, but existing methods rely on expensive sensors or computationally expensive algorithms. Additionally, there is no existing dataset to evaluate point cloud change detection. Thus, this paper proposes a novel framework using low-cost sensors like stereo cameras and IMU to detect changes in a point cloud map. Moreover, we create a dataset and the corresponding metrics to evaluate point cloud change detection with the help of the high-fidelity simulator Unreal Engine 4. Experiments show that our visual-based framework can effectively detect the changes in our dataset.

I. INTRODUCTION

Autonomous ground and unnamed aerial vehicles have become popular over the last few years. These robotic vehicles are commonly used in various tasks, such as logistics delivery and remote sensing, with localization and navigation being mandatory sub-tasks requiring an accurate and up-to-date map. Thus, detecting the map changes is crucial.

This work exploits crowdsourced data to detect map changes in real-time. Crowdsourced data is collected from several vehicles equipped with sensors like a camera, and the location where vehicles pass also contributes to detecting map changes. When many vehicles collect data, the overall sensor cost and the collected data are enormous. Hence, these vehicles should be equipped with low-cost sensors to reduce hardware costs, and crowdsourced data should be processed using an algorithm with low computational complexity.

Current change detection methods utilize an expensive hardware setup. For example, remote sensing tasks utilize expensive sensors like vehicle-based laser scanner (VLS), airborne laser scanner (ALS), and mobile laser scanner (MLS) to detect point cloud changes [1]–[3]. However, the price of a laser scanner ranges from thousands to millions of dollars. Alternative solutions exploit the structure from motion (SfM), and multi-view stereo (MVS) technology [4], but these methods impose a huge computational complexity,

typically requiring several hours to days of calculations, depending on the point cloud size. For example, Yew *et.al* [4] developed a SfM-based algorithm, where the reconstruction and registration steps need three days for a medium-size urban environment.

Considering the available datasets, EuRoC [5] and KITTI [6], and their corresponding metrics focus on evaluating the performance of localization and mapping. Moreover, the SHREC 2021 point cloud change detection dataset [7] focuses on change detection of point clouds collected by LiDAR. Hence, to the best of our knowledge, datasets and metrics to evaluate visual-based point cloud change detection do not exist, and thus evaluating the performance of change detection is a challenging task.

Hence, this paper proposes a novel visual-based framework to achieve low-cost change detection in point clouds and a dataset with the appropriate metrics to evaluate the performance of point cloud change detection. The main contributions of this paper are as follows:

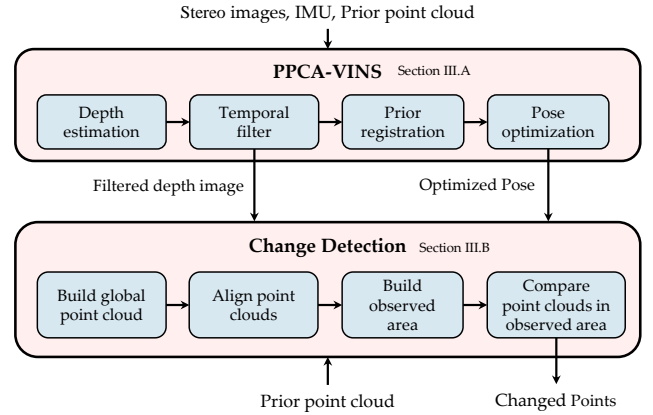


Fig. 1. Proposed change detection framework comprising the PPCA-VINS and Change Detection modules. PPCA-VINS provides 6D poses and depth images for change detection, which are then input to the change detection pipeline to build a global point cloud. Then the global point cloud and the prior point clouds of an observed area are compared, with the change detection pipeline providing the point cloud vertices that have changed.

¹Department of Electronic Engineering, Tsinghua University, Beijing, 100084, China. jian-wang@tsinghua.edu.cn, lzh20@mails.tsinghua.edu.cn

²Meituan, 7 Rongda Road, Chaoyang District, Beijing, 100012, China.

This research was supported by National Natural Science Foundation of China (U20A20334, U19B2019 and M-0248), Tsinghua-Meituan Joint Institute for Digital Life, Tsinghua EE Independent Research Project, Beijing National Research Center for Information Science and Technology (BNRist), and Beijing Innovation Center for Future Chips.

Our code is in the repository: <https://github.com/lxexen1/PPCA-VINS.git>, and dataset is also released on this page.

- Proposing a prior point cloud-assisted SLAM framework named PPCA-VINS (prior point cloud-assisted VINS), based on VINS-Fusion [8] and assuming having an accurate initial pose. Compared to standard VINS-Fusion, our frame fuses prior information from a prior point clouds and affords an appealing performance over the standard VINS-Fusion on our dataset.
- Designing a new *dataset and the corresponding metrics*

for visual-based point cloud change detection tasks. The dataset fills the vacancy in the point cloud change detection task and provides raw data from multiple sensor types onboard a car or an unnamed aerial vehicle.

- Developing a visual-based change detection architecture that utilizes depth images and poses provided by PPCA-VINS to build a global point cloud. We detect changes by comparing the global point cloud to the prior point cloud. Our change detection pipeline is evaluated on our change detection dataset, verifying its capability for point cloud change detection.

The proposed framework is illustrated in Fig 1 and comprises two parts. The first part is PPCA-VINS (Section III-A), which estimates depth from stereo images and then builds filtered depth images. Then we convert the filtered depth image to a point cloud and register it to the previous point cloud. Finally, we optimize the vehicle’s pose by fusing the pose obtained from VINS-Fusion and the prior registration.

The second part of our architecture is the change detection module (Section III-B). In this module, we first build a global point cloud using the filtered depth images and optimized poses from PPCA-VINS, and then we align the global point cloud to the prior point clouds. Then we build the point cloud of the observed area and compare the global point cloud to the prior point clouds using point cloud registration to obtain the changed vertices.

The remainder of this paper is as follows: Section II presents the related work, while Section III includes the proposed method. Section IV builds the suggested dataset using the high-fidelity simulator Unreal Engine 4 [9] due to ease of changing environment and data collection. Moreover, this section suggests some evaluation metrics. Section V conducts several experiments to demonstrate the framework’s and dataset’s effectiveness on map change detection tasks using low-cost sensors and algorithms. Finally, section VI concludes this work.

II. RELATED WORK

A. Visual Locating with Prior Map

Visual localization has been researched for several years. For example, Zuo *et al.* [10] proposed a tightly-coupled MSCKF [11] scheme using stereo vision. In this work, the local point clouds were generated from a stereo camera setup and utilized NDT [12] to align the local point clouds and the prior LiDAR map, where the location in the prior map was considered as a state in the MSCKF’s extended Kalman filter. Lynen *et al.* [13] developed a pipeline based on SfM. This method was also MSCKF-based and tightly coupled. The difference between [13] and [10] is the prior locating algorithm, as [13] employed SfM to generate the prior point cloud map and stored the visual landmark descriptors as a database in the meantime. The descriptors obtained from the images were calculated and matched against the database landmarks, and then the pose relationship between the 2D feature point and 3D landmarks was filtered using an extended Kalman filter to obtain the final pose estimation.

Li *et al.* [14] suggested a deep learning method named DeepI2P to register images to point clouds. In this work, the authors converted the cross-modal registration problem into a classification problem, where a deep neural network is trained to classify whether a point in a point cloud is within the image frustum. In that case, a post-optimization method is applied to estimate the images’ poses.

B. Point Cloud Change Detection

Yew *et al.* [4] combined SfM and neural networks, where the SfM built a global point cloud and the neural network performed non-rigid registration between the point clouds. The author claimed that “our BD dataset requires 3 days 25 min, and 2 min respectively for the reconstruction, registration, and change detection steps.”, which highlights that SfM-based methods are extremely time-consuming. In addition, this method did not distinguish the unknown and empty areas. Xu *et al.* [15] utilized ALS and octrees. Specifically, this method collected point clouds utilizing ALS and the octree stored and indexed the irregularly-distributed points. Then, the points were clustered and classified into different kinds, followed by a registration process to reveal the changed areas. Although this work did not distinguish between unknown and empty areas, it is reasonable to assume that collecting LiDAR data from airborne sensors do not produce many unknown areas.

This work employs VINS-Fusion, a unified framework for pose estimation, to provide the VIO pose for our pipeline. Besides tightly-coupled sensors (camera, IMU), many other sensors can be loosely coupled into our framework, making our development more straightforward. We consider the registered pose from a prior map as an output from a virtual sensor, combined with the VIO pose to obtain a globally optimized pose. In addition, MSCKF and VINS-Fusion use a sliding window to reduce processing time. Thus a tightly-coupled VIO requires a quick registration between the local and the prior point clouds—otherwise, the keyframe is discarded from the sliding window. Opposing current works, the proposed method relies exclusively on cheap sensors like stereo camera, GPS and IMU. Moreover, our pipeline is computationally efficient; thus, our entire framework is low-cost.

III. FRAMEWORK

A. PPCA-VINS

1) *Depth Estimation:* VINS-Fusion can track feature points and generate a sparse point cloud from these points. However, using a sparse point cloud does not provide an accurate localization result through registration. Thus, additional work producing a semi-dense point cloud is expected.

One standard method of cross-modal data processing is converting different modalities into one. In our pipeline, we convert stereo images into point clouds, as stereo depth estimation has been a popular research topic for several years. Semi-global matching (SGM) [16] is a classic method for disparity estimation, based on minimizing the mutual

information (MI) between two images. Recently, many neural networks (NNs) based on stereo depth estimation methods have emerged, such as PSMNet [17] and AnyNet [18]. However, these methods have a significant time complexity, and the depths produced are not better than the traditional SGM method. Thus, we leverage SGM to produce depth estimation for stereo images.

2) *Temporal Filter*: The depth images produced by SGM incorporate significant noise. Thus, we adopt the temporal filter proposed in [19] and a similar method named *depth correspondence matching* [10]. We follow these methods and implement a simplified version of the temporal filter.

Let the current keyframe be i . We re-project the estimated depth of every pixel (u, v) in keyframe j ($i - 2 \leq j \leq i + 2, j \neq i$) to the current keyframe i and obtain the projected depth $d_j^i(u, v)$ and pixel coordinate (u', v') . If the distance between the projected depth $d_j^i(u, v)$ and the current frame depth $d_i(u', v')$ is smaller than a threshold δ_d , we call this a successful projection. When a pixel is successfully projected over α times, we average the projected depth and the current frame depth of this pixel to obtain a filtered depth, which is added to the filtered depth image.

3) *Prior Registration*: We increase the point cloud's density by aggregating the point cloud of every five keyframes to a local cloud, producing a denser point cloud.

For our pipeline, we need to register two point clouds, each including tens of thousands of points. Thus, we need a fast and accurate registration algorithm. Normal distribution transform (NDT) [12] is a processing efficient registration algorithm, which is unsuitable for our pipeline, as it often produces results suffering from a considerable drift. Alternatively, the iterative closest point (ICP) [20] is an accurate registration algorithm but it requires much time even to align two small point clouds. Besides, the Generalized ICP (GICP) [21] is an improved ICP-based algorithm that balances speed and accuracy. Koide *et al.* [22] boosted GICP by implementing the algorithm on multiple threads. Indeed, we conducted several tests comparing a 4-threaded GICP and other single threaded algorithms involving a point cloud and its variant translated by 0.2m. The corresponding results are reported in Table I revealing the superiority of the 4-threaded GICP. Hence, in our pipeline we apply GICP with 4 threads.

TABLE I
COMPARISON OF DIFFERENT REGISTRATION ALGORITHMS

| Algorithm | Time Consumption (s) | Error (m) |
|-----------------|----------------------|-----------|
| ICP | 1.305 | 0.0062 |
| NDT | 0.270 | 0.0136 |
| GICP | 1.250 | 0.0062 |
| GICP(4 threads) | 0.436 | 0.0062 |

Registration is not always accurate, and therefore we evaluate the registration results using the fitness metric, which is the mean distance from each point in the local cloud to its closest point in the prior cloud. We evaluate

every registration based on the following:

- 1) Registration should be converged.
- 2) Fitness of registration should be less than a threshold.
- 3) Registration's translation length should be less than a threshold.

Note that GICP is formulated as a Maximum-Likelihood Estimation (MLE) problem, so the Hessian matrix in the GICP registration is the negative of the Fisher information matrix. The registration's covariance matrix is the inverse of the Fisher information matrix, written as follows:

$$\text{cov}(\theta) = \mathcal{I}^{-1}(\theta) = (-\mathbf{H}_\theta)^{-1} \quad (1)$$

The covariance matrix is used in the following global pose estimation.

4) *Pose Optimization*: When the point cloud registration process completes, a global pose optimization process is activated utilizing the VIO pose. The prior localization states considering the prior position and orientation of the k -th keyframe are:

$$\mathbf{p}_k^p, \mathbf{q}_k^p \quad (2)$$

In VINS-Fusion, the global pose graph optimization problem is modelled as a maximum likelihood estimation (MLE) problem. The variables to be optimized are global poses:

$$\mathcal{X} = [\mathbf{x}_0, \mathbf{x}_1, \dots, \mathbf{x}_n] \quad (3)$$

$$\mathbf{x}_k = [\mathbf{p}_k, \mathbf{q}_k], k \in [0, n] \quad (4)$$

Assuming that the measurement uncertainties are Gaussian distributions, the problem is formulated as :

$$\mathcal{X}^* = \arg \max_{\mathcal{X}} \prod_{t=0}^n \prod_{k \in \mathcal{S}} p(\mathbf{z}_t^k | \mathcal{X}) \quad (5)$$

$$= \arg \min_{\mathcal{X}} \sum_{t=0}^n \sum_{k \in \mathcal{S}} \|\mathbf{z}_t^k - h_t^k(\mathcal{X})\|_{\Omega_t^k}^2 \quad (6)$$

Since we use the same VIO factor as in the VINS-Fusion's original paper, we do not explain it here to enhance readability. Considering the prior localization factor, we divide it into two parts. One is the global position factor:

$$\mathbf{z}_t^p - h_t^p(\mathcal{X}) = \mathbf{z}_t^p - h_t^p(\mathbf{x}_t) = \mathbf{p}_t^p - \mathbf{p}_t \quad (7)$$

and the other one is the relative rotation factor from frame one to current frame t :

$$\mathbf{z}_t^q - h_t^q(\mathcal{X}) = \mathbf{z}_t^q - h_t^q(\mathbf{x}_1, \mathbf{x}_t) = (\mathbf{q}_1^p)^{-1} \mathbf{q}_t^p \quad (8)$$

Considering the prior localization factor, we build a pose graph and optimize it to obtain the global pose. The covariance of the prior localization is given in eq.1, which is used to calculate the confidence of the prior localization.

B. Change Detection

This subsection builds a simple change detection algorithm that comprises the following steps:

- 1) build the global point cloud \mathcal{P}_g
- 2) align the global point cloud to the prior point cloud \mathcal{P}_p

- 3) build the observed area \mathcal{A}_{obs}
- 4) build the observed prior point cloud (\mathcal{P}_p^{obs}) and compare \mathcal{P}_p^{obs} and \mathcal{P}_g

Initially, we use the keyframes' 6D pose and filtered depth image to build a global point cloud. Then we register the global point cloud to the prior point cloud to align the two clouds.

In step 3, we must know what part of the point cloud has been observed to determine the part of the point cloud that has changed. So we leverage the octomap of resolution ρ_o to build an observed area \mathcal{A}_{obs} . For the pixels in the filtered depth image with a depth small than th_d , we cast a ray from the camera to the point. For those pixels without a depth, we also cast a ray from the camera with a certain depth th_f to add some free space to octomap. The optimal value of th_f is experimentally defined.

In step 4, we build the observed prior point cloud \mathcal{P}_p^{obs} . Given the depth estimation inaccuracy, we use distance to \mathcal{P}_g to judge whether a point of \mathcal{P}_p is observed. So we consider a point of \mathcal{P}_p is observed when it is in \mathcal{A}_{obs} or is within a distance th_{ch} of \mathcal{P}_g , as shown in Algorithm 1.

Finally, we compare the point clouds by calculating the point-to-cloud distance between \mathcal{P}_g and \mathcal{P}_p^{obs} . If a point in \mathcal{P}_g is not within a distance th_{ch} of \mathcal{P}_p^{obs} , we classify this point as a new point. If a point in \mathcal{P}_p^{obs} is not within a distance th_{ch} of \mathcal{P}_g , we classify this point as a removed point. Finally, a set of new points \mathcal{P}_{new} and a set of removed points \mathcal{P}_{rm} are built, as shown in Algorithm 2.

Algorithm 1: Building the observed prior point cloud

Data: $\mathcal{P}_p, \mathcal{P}_g, \mathcal{A}_{obs}, th_{ch}$
Result: Observed prior point cloud \mathcal{P}_p^{obs}
for $p \in \mathcal{P}_p$ **do**
 if $p \in \mathcal{A}_{obs}$ **or** $calcNearestDist(pt, \mathcal{P}_g) \leq th_{ch}$ **then**
 $\mathcal{P}_p^{obs}.append(p)$

Algorithm 2: Classification of points

Data: $\mathcal{P}_g, \mathcal{P}_p^{obs}$
Result: $\mathcal{P}_{new}, \mathcal{P}_{rm}$
for $p \in \mathcal{P}_g$ **do**
 if $calcNearestDist(p, \mathcal{P}_p^{obs}) \geq th_{ch}$ **then**
 $\mathcal{P}_{new}.append(p)$
for $p \in \mathcal{P}_p^{obs}$ **do**
 if $calcNearestDist(p, \mathcal{P}_g) \geq th_{ch}$ **then**
 $\mathcal{P}_{rm}.append(p)$

IV. DATASET AND METRICS

A. Dataset

To evaluate our change detection pipeline, we build a dataset using the simulated environment in Unreal Engine

4 with the AirSim [23] plugin. The simulated dataset affords quickly changing environments and collecting data in a simulated world. We have built three environments in good light condition, namely the original environment and two changed environments (in each one we remove a building and add a new building (Fig 2)). Each environment has a size of $250 \times 250 \times 40$ meters (length \times width \times height), and for each scene, we also build its ground truth point cloud.

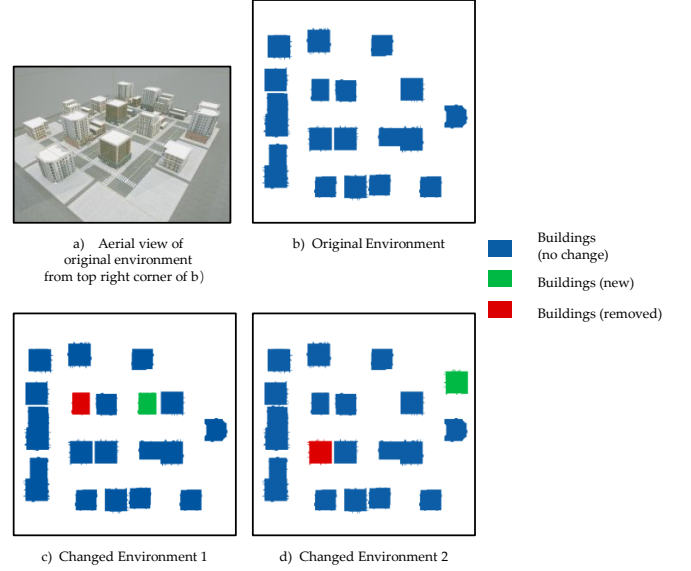


Fig. 2. Aerial view of the original environment and top views of the three environments. Blue for unchanged buildings, green for new buildings, and red for removed buildings.

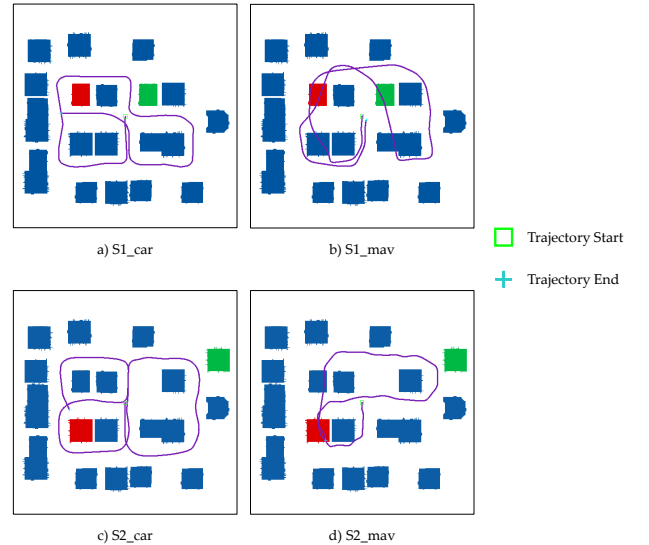


Fig. 3. Top view of the trajectories. Purple for trajectory, green rectangle for starting point and cyan cross for ending point.

In every scene, we record a car's, and a MAV's trajectory (Fig 3) recorded with 30 Hz 800×450 stereo pairs, 200 Hz IMU and ground truth 6D pose data. The stereo pairs and

IMU are noiseless. Table II reports some brief information on the trajectories. Prefix "S1" and "S2" denote the "Changed Environment 1" and "Changed Environment 2".

TABLE II
BRIEF TRAJECTORY INFORMATION IN OUR CHANGE DETECTION DATASET

| Trajectory | Time (s) | Length (m) | Vehicle type |
|------------|----------|------------|--------------|
| S1_car | 181.01 | 641.56 | car |
| S1_mav | 173.93 | 795.00 | mav |
| S2_car | 194.00 | 758.00 | car |
| S2_mav | 162.99 | 513.78 | mav |

Algorithm 3: Build clouds from the true positive points

Data: $\mathcal{P}_{p,rm}^{obs}, \mathcal{P}_{p,new}^{obs}, \mathcal{P}_{rm}, \mathcal{P}_{new}$
Result: $\mathcal{P}_{p,rm}^{obs,TP}, \mathcal{P}_{p,new}^{obs,TP}, \mathcal{P}_{rm}^{TP}, \mathcal{P}_{new}^{TP}$
for $p \in \mathcal{P}_{p,rm}^{obs}$ **do**
 if $\text{calcNearestDist}(p, \mathcal{P}_{rm}) \leq th_{ch}$ **then**
 $\mathcal{P}_{p,rm}^{obs,TP}.\text{append}(p)$
for $p \in \mathcal{P}_{p,new}^{obs}$ **do**
 if $\text{calcNearestDist}(p, \mathcal{P}_{new}) \leq th_{ch}$ **then**
 $\mathcal{P}_{p,new}^{obs,TP}.\text{append}(p)$
for $p \in \mathcal{P}_{rm}$ **do**
 if $\text{calcNearestDist}(p, \mathcal{P}_{p,rm}^{obs}) \leq th_{ch}$ **then**
 $\mathcal{P}_{rm}^{TP}.\text{append}(p)$
for $p \in \mathcal{P}_{new}$ **do**
 if $\text{calcNearestDist}(p, \mathcal{P}_{p,new}^{obs}) \leq th_{ch}$ **then**
 $\mathcal{P}_{new}^{TP}.\text{append}(p)$

B. Metrics

In our pipeline, the changed area is presented as a point cloud. Hence, we consider the change detection problem as a classification problem of points, and therefore, we introduce some standard classification metrics to the change detection problem.

We employ the following metrics for change detection evaluation:

- 1) Recall of class new: R_{new}
- 2) Precision of class new: P_{new}
- 3) Recall of class removed: R_{rm}
- 4) Precision of class removed: P_{rm}

Besides, we denote $N(\cdot)$ as the number of points in a point cloud.

To evaluate the algorithms on the same standards, all point clouds are downsampled to a certain resolution ρ_p . In our paper, $\rho_p = 0.4m$.

We must know the prior new and the removed points to calculate these metrics. Hence, in our change detection algorithm, we use the same algorithm as in Algorithm 2. Specifically, we replace $\mathcal{P}_g, \mathcal{P}_p^{obs}$ with the prior point cloud of the changed and the original scene, and the algorithm outputs prior new points $\mathcal{P}_{p,new}$ and the prior removed points $\mathcal{P}_{p,rm}$ of the changed scene.

Similarly, for the change detection algorithms, we must know which points are observed in the prior new points and prior removed points. To obtain these points, we replace \mathcal{P}_p with $\mathcal{P}_{p,new}$ and $\mathcal{P}_{p,rm}$ in Algorithm1 and obtain the observed prior new and removed points $\mathcal{P}_{p,new}^{obs}, \mathcal{P}_{p,rm}^{obs}$.

Superscript "TP" marks the point cloud with correctly classified points. For example, \mathcal{P}_{rm}^{TP} means points in \mathcal{P}_{rm} that are within a distance th_{ch} of $\mathcal{P}_{p,rm}^{obs}$, as presented in Algorithm 3.

Thus the metrics can be written as:

$$R_{new} = \frac{N(\mathcal{P}_{p,new}^{obs,TP})}{N(\mathcal{P}_{p,new}^{obs})}, \quad P_{new} = \frac{N(\mathcal{P}_{new}^{TP})}{N(\mathcal{P}_{new})} \quad (9)$$

$$R_{rm} = \frac{N(\mathcal{P}_{p,rm}^{obs,TP})}{N(\mathcal{P}_{p,rm}^{obs})}, \quad P_{rm} = \frac{N(\mathcal{P}_{rm}^{TP})}{N(\mathcal{P}_{rm})} \quad (10)$$

Besides, we challenge our dataset against other point cloud change detection datasets like the SHREC 2021 [7] and the dataset built by Gélis *et al.* [24]. The corresponding results are reported in Table III.

TABLE III
COMPARISON OF POINT CLOUD CHANGE DETECTION DATASETS

| Dataset | Environment type | Sensor |
|--------------------------|------------------|--------------------|
| Ours | simulated urban | Stereo camera, IMU |
| SHREC 2021 [7] | real urban | LiDAR |
| Gélis <i>et al.</i> [24] | simulated urban | LiDAR |

| Dataset | Vehicle type | Metrics |
|---------------------|----------------|--------------------------------------|
| Ours | ground, aerial | recall, precision of points' classes |
| SHREC 2021 | ground | accuracy, IoU of objects' classes |
| Gélis <i>et al.</i> | aerial | IoU of points' classes |

V. EXPERIMENTAL RESULTS

Our experiments can be divided into two parts: First, the prior locating test shows our PPCA-VINS's advantage over no prior information-assisted methods. Second, the change detection test demonstrates that our change detection dataset and metrics can effectively evaluate a change detection algorithm and that our visual-based baseline pipeline works successfully on the dataset.

In addition, in our experiment we assume that we have an accurate initial guess of the vehicle's pose. Finally, all experiments are conducted on a desktop PC with an Intel i9-11900K, an Nvidia RTX 3090, and 32 GB RAM.

A. Prior Localization Test

1) *EuRoC MAV Dataset*: EuRoC MAV Dataset [5] is an indoor dataset containing 20Hz stereo camera images, 200Hz IMU, ground truth 6D pose, and ground truth laser scan data (prior LiDAR map). Hence, this dataset is suitable for the prior locating test. The raw stereo camera image in the EuRoC dataset is unrectified. However, stereo matching requires rectified image pairs, and therefore, we use the calibration and rectification parameters provided by ORB-SLAM2 [25] to rectify the image pairs first. Then the prior LiDAR map is downsampled to a resolution of 5 cm. We assume that we have an accurate initial pose of MAV, and we simultaneously perform VIO localization and prior map-assisted localization.

Since our work is based on the state-of-the-art SLAM frame VINS-Fusion, we compare our work against the VINS-Fusion. Considering the evaluation metrics, we leverage Evo [26] to calculate the root mean squared error (RMSE) and standard deviation (STD) of the absolute trajectory error (ATE). To avoid randomness during feature tracking and keyframe selection, we perform each method five times on one trajectory and calculate the average RMSE and STD of ATE. Depending on the trajectory, our configuration slightly differs, with the related code available in our Github repository. The corresponding results are reported in Table IV.

TABLE IV
AVERAGE RMSE (M) AND STD (M) OF ATE ON EUROC FOR PPCA-VINS AND VINS-FUSION

| Trajectory | PPCA-VINS | | VINS-Fusion | |
|-----------------|-----------|--------|-------------|--------|
| | RMSE | STD | RMSE | STD |
| V1_01_easy | 0.1464 | 0.0197 | 0.1470 | 0.0231 |
| V1_02_medium | 0.0904 | 0.0232 | 0.1170 | 0.0448 |
| V1_01_difficult | 0.1372 | 0.0393 | 0.1859 | 0.0576 |
| V2_01_easy | 0.1785 | 0.1001 | 0.1790 | 0.1013 |
| V2_02_medium | 0.1603 | 0.0678 | 0.1690 | 0.0760 |
| V2_03_difficult | 0.2387 | 0.1080 | 0.2445 | 0.1095 |

Our PPCA-VINS performs better than VINS-Fusion on every trajectory ranging from easy to difficult. Hence, our method is more appealing than the standard VINS-Fusion affording a higher localization accuracy and a more stable trajectory error. However, our method's performance on trajectory V2_03_difficult is inferior to V1_03_difficult because the former trajectory is more dynamic and recorded in darker light conditions, limiting our point cloud generation scheme and creating more noise in our prior locate result.

2) *Change Detection Dataset*: We also compare our work to the standard VINS-Fusion on our dataset. Unlike the EuRoC dataset, our change detection dataset is collected in outdoor scenes, and thus we use the original scene's point cloud as the prior point cloud in PPCA-VINS. This means that we use an outdated point cloud as prior information.

Each trajectory is tested five times, and the metrics are averaged over five runs. The corresponding results are presented in Table V, highlighting that even with an outdated prior point cloud, PPCA-VINS performs much better on each trajectory than the standard VINS-Fusion. Moreover, the results reveal that our method can successfully run on both car and MAV platforms.

TABLE V
AVERAGE RMSE (M), STANDARD DEVIATION (M), AND MAXIMUM (M) OF ATE ON OUR DATASET FOR PPCA-VINS AND VINS-FUSION

| Trajectory | PPCA-VINS | | | VINS-Fusion | | |
|------------|-----------|--------|--------|-------------|--------|--------|
| | RMSE | STD | MAX | RMSE | STD | MAX |
| S1_car | 0.7484 | 0.3255 | 1.3218 | 1.2509 | 0.4900 | 2.1392 |
| S1_mav | 0.9781 | 0.3938 | 1.8866 | 2.5852 | 1.0330 | 4.2434 |
| S2_car | 0.4323 | 0.2185 | 1.5728 | 0.7749 | 0.4240 | 2.4654 |
| S2_mav | 0.9942 | 0.5503 | 2.2049 | 1.4180 | 0.5026 | 2.2547 |

B. Change Detection Test

In this section, we employ our suggested change detection dataset and set th_{ch} to 2.4 m, ρ_o to 0.8 m, and all point clouds are downsampled to 0.4m.

1) *Free Space Ray Casting Test*: As mentioned in III-B, for pixels in filtered depth images that have an empty depth value, we cast a ray from the camera to depth th_f . This section evaluates various th_f depths to determine the optimal value.

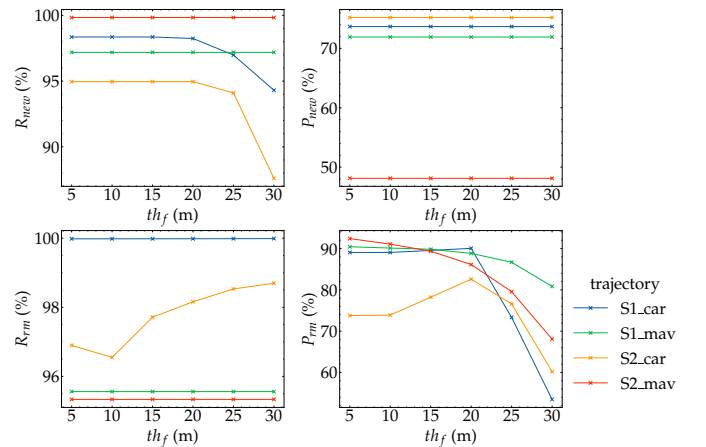


Fig. 4. Recall and precision results of different classes when free space ray casting depth th_f has various values.

We set th_f to 5, 10, 15, 20, 25, and 30 m and calculate the recall and precision metrics in IV-B to determine the

best th_f value. This experiment utilizes the 6D pose and the corresponding filtered depth image from PPCA-VINS. Each metric is averaged over five runs. Fig 4 illustrates the results revealing that th_f has a great influence on P_{rm} .

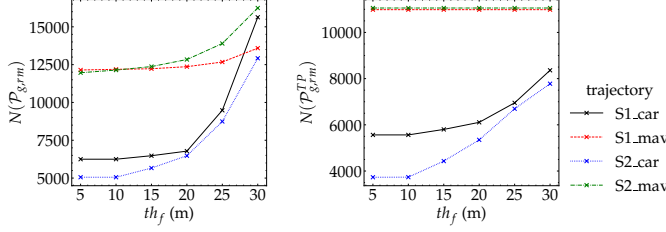


Fig. 5. $N_{P_{rm}}$ and $N_{P_{rm}^{TP}}$ of different classes when free space ray casting depth th_f has various values.

As presented in Fig 5, for trajectories recorded from a car, when th_f increases more areas with removed points are observed. Thus P_{rm} slightly increases when th_f is less than 20 m. For all trajectories, when th_f exceeds 20 m, $N(P_{rm})$ increases rapidly, but $N(P_{rm}^{TP})$ increases much slower than $N(P_{rm})$, inferring that when th_f is too large, many unobserved are considered as observed, causing a significant reduction in P_{rm} . Besides, R_{new} also drops when th_f increases for the same reason.

As presented in the figures above, setting th_f to 15 or 20 meters attains the best performance. Thus, in the subsequent section we set th_f to 20 meters.

2) *Comparison of Metrics using Different Pose Estimations*: This section calculates the metrics mentioned above with the 6D poses calculated from our method and the standard VINS-Fusion. The metrics are calculated for every trajectory and are averaged over five runs.

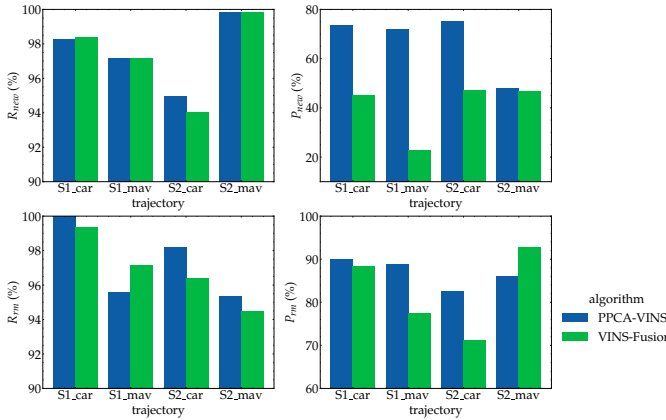


Fig. 6. Comparison of the change detection results using 6D poses from PPCA-VINS and VINS-Fusion.

Fig 6 highlights that PPCA-VINS affords a better performance on nearly every trajectory and metric, especially on P_{new} , indicating that our dataset and metrics are successful on point cloud change detection tasks. Besides, our visual-based baseline pipeline is verified effective on point cloud change detection tasks, affording a high recall on both new and removed points.

Moreover, we find the P_{new} is significantly lower than P_{rm} and P_{new} is heavily influenced by the pose estimation accuracy. Indeed, when the estimated error increases, the re-projected point cloud from the camera to the real world drifts more, leading to a wrongly estimated observed area and imposing more re-projected points to be falsely classified as new points. P_{rm} is related to the prior point cloud and observed area. If the pose error is less than th_{ch} , the prior points in the wrongly observed area will also be within the threshold th_{ch} of our global point clouds. Besides, in our environment, free space is much more than space occupied by buildings. So a minor drift very likely leads vehicles from observing a free area to observing another free space, which has a minor impact on the final metrics.

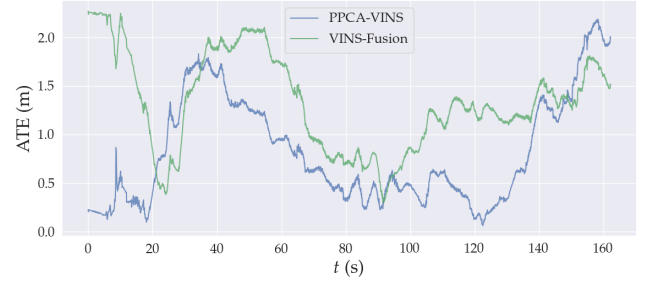


Fig. 7. ATE (m) of PPCA-VINS and VINS-Fusion of one trial on trajectory S2_mav

We also find that our PPCA-VINS does not outperform VINS-Fusion on trajectory S2_mav, so we plot the corresponding ATE to investigate the reason. Considering the other trajectories, the ATE of PPCA-VINS is always lower than VINS-Fusion, and the maximum of PPCA-VINS's ATE is also significantly lower than that of VINS-Fusion. Thus, the PPCA-VINS poses produce better results. However, for trajectory S2_mav, the ATE of PPCA-VINS is not always lower than VINS-Fusion, and the maximum ATE of PPCA-VINS is close to that of VINS-Fusion (Table V, Fig 7). So both algorithms produces similar results on trajectory S2_mav.

C. Processing Time

Our baseline framework is processing efficient, as on our PC, PPCA-VINS completes every trajectory of our dataset in 240 seconds (each environment in our dataset has a size of $250m \times 250m \times 40m$). For the change detection pipeline, building point cloud having new and removed points requires less than five minutes per trajectory. Compared to Lidar-based and SfM-based methods, the proposed method has the advantages of relying on low-cost hardware and affords a low computational complexity.

VI. CONCLUSIONS AND FUTURE WORK

This paper proposes a novel visual-based point change detection pipeline and a simple simulated point change detection dataset and corresponding metrics. Compared to not employing a prior map, our PPCA-VINS achieves a higher

pose estimation accuracy and better point cloud change detection results. Our visual-based point cloud change detection pipeline achieves an appealing result on our dataset, and the point cloud change detection metrics represent the corresponding performance efficiently.

Future work will investigate change detection in more complicated environments involving moving objects, small objects like bushes, and poor light conditions. Moreover, we will conduct some real-world indoor tests.

REFERENCES

- [1] J. Hyypä, A. Jaakkola, H. Hyypä, H. Kaartinen, A. Kukko, M. Holopainen, L. Zhu, M. Vastaranta, S. Kaasalainen, A. Krooks, P. Litkey, P. Lyytikäinen-Saarenmaa, L. Matikainen, P. Ronnholm, R. Chen, Y. Chen, A. Kivilahti, and I. Kosonen, "Map updating and change detection using vehicle-based laser scanning," in *2009 Joint Urban Remote Sensing Event*, 2009, pp. 1–6.
- [2] H. Murakami, K. Nakagawa, H. Hasegawa, T. Shibata, and E. Iwanami, "Change detection of buildings using an airborne laser scanner," *ISPRS Journal of Photogrammetry and Remote Sensing*, vol. 54, no. 2-3, pp. 148–152, 1999.
- [3] R. Qin and A. Gruen, "3d change detection at street level using mobile laser scanning point clouds and terrestrial images," *ISPRS Journal of Photogrammetry and Remote Sensing*, vol. 90, pp. 23–35, 2014.
- [4] Z. J. Yew and G. Hee Lee, "City-scale scene change detection using point clouds," in *IEEE International Conference on Robotics and Automation (ICRA)*, 2021, pp. 13 362–13 369.
- [5] M. Burri, J. Nikolic, P. Gohl, T. Schneider, J. Rehder, S. Omari, M. W. Achtelik, and R. Siegwart, "The euroc micro aerial vehicle datasets," *The International Journal of Robotics Research*, 2016. [Online]. Available: <http://ijr.sagepub.com/content/early/2016/01/21/0278364915620033.abstract>
- [6] A. Geiger, P. Lenz, and R. Urtasun, "Are we ready for autonomous driving? the kitti vision benchmark suite," in *Conference on Computer Vision and Pattern Recognition (CVPR)*, 2012.
- [7] T. Ku, S. Galanakis, B. Boom, R. C. Veltkamp, D. Bangera, S. Gangisetty, N. Stagakis, G. Arvanitis, and K. Moustakas, "Shrec 2021: 3d point cloud change detection for street scenes," *Comput. Graph.*, vol. 99, no. C, p. 192–200, oct 2021. [Online]. Available: <https://doi.org/10.1016/j.cag.2021.07.004>
- [8] T. Qin, S. Cao, J. Pan, and S. Shen, "A general optimization-based framework for global pose estimation with multiple sensors," 2019. [Online]. Available: <http://arxiv.org/abs/1901.03642>
- [9] Epic Games, "Unreal engine." [Online]. Available: <https://www.unrealengine.com>
- [10] X. Zuo, P. Geneva, Y. Yang, W. Ye, Y. Liu, and G. Huang, "Visual-inertial localization with prior lidar map constraints," *IEEE Robotics and Automation Letters*, vol. 4, no. 4, pp. 3394–3401, 2019.
- [11] A. I. Mourikis and S. I. Roumeliotis, "A multi-state constraint kalman filter for vision-aided inertial navigation," in *Proceedings 2007 IEEE International Conference on Robotics and Automation*, 2007, pp. 3565–3572.
- [12] M. Magnusson, "The three-dimensional normal-distributions transform: an efficient representation for registration, surface analysis, and loop detection," Ph.D. dissertation, Örebro universitet, 2009.
- [13] S. Lynen, T. Sattler, M. Bosse, J. Hesch, M. Pollefeys, and R. Siegwart, "Get out of my lab: Large-scale, real-time visual-inertial localization," in *Robotics: Science and Systems*, 2015.
- [14] J. Li and G. H. Lee, "Deepi2p: Image-to-point cloud registration via deep classification," in *Proceedings of the IEEE/CVF Conference on Computer Vision and Pattern Recognition (CVPR)*, June 2021, pp. 15 960–15 969.
- [15] H. Xu, L. Cheng, M. Li, Y. Chen, and L. Zhong, "Using octrees to detect changes to buildings and trees in the urban environment from airborne lidar data," *Remote Sensing*, vol. 7, no. 8, pp. 9682–9704, 2015.
- [16] H. Hirschmuller, "Accurate and efficient stereo processing by semi-global matching and mutual information," in *2005 IEEE Computer Society Conference on Computer Vision and Pattern Recognition (CVPR'05)*, vol. 2, 2005, pp. 807–814 vol. 2.
- [17] J. Chang and Y. Chen, "Pyramid stereo matching network," *CoRR*, vol. abs/1803.08669, 2018. [Online]. Available: <http://arxiv.org/abs/1803.08669>
- [18] Y. Wang, Z. Lai, G. Huang, B. H. Wang, L. Van Der Maaten, M. Campbell, and K. Q. Weinberger, "Anytime stereo image depth estimation on mobile devices," *arXiv preprint arXiv:1810.11408*, 2018.
- [19] S. Matyunin, D. Vatolin, Y. Berdnikov, and M. Smirnov, "Temporal filtering for depth maps generated by kinect depth camera," in *2011 3DTV Conference: The True Vision - Capture, Transmission and Display of 3D Video (3DTV-CON)*, 2011, pp. 1–4.
- [20] P. Besl and N. D. McKay, "A method for registration of 3-d shapes," *IEEE Transactions on Pattern Analysis and Machine Intelligence*, vol. 14, no. 2, pp. 239–256, 1992.
- [21] A. Segal, D. Haehnel, and S. Thrun, "Generalized-icp," in *Robotics: science and systems*, vol. 2, no. 4. Seattle, WA, 2009, p. 435.
- [22] K. Koide, M. Yokozuka, S. Oishi, and A. Banno, "Voxelized gicp for fast and accurate 3d point cloud registration," in *2021 IEEE International Conference on Robotics and Automation (ICRA)*, 2021, pp. 11 054–11 059.
- [23] S. Shah, D. Dey, C. Lovett, and A. Kapoor, "Airsim: High-fidelity visual and physical simulation for autonomous vehicles," in *Field and Service Robotics*, 2017. [Online]. Available: <https://arxiv.org/abs/1705.05065>
- [24] I. de Gélis, S. Lefèvre, and T. Corpetti, "Change detection in urban point clouds: An experimental comparison with simulated 3d datasets," *Remote Sensing*, vol. 13, no. 13, 2021. [Online]. Available: <https://www.mdpi.com/2072-4292/13/13/2629>
- [25] R. Mur-Artal and J. D. Tardós, "Orb-slam2: An open-source slam system for monocular, stereo, and rgb-d cameras," *IEEE Transactions on Robotics*, vol. 33, no. 5, pp. 1255–1262, 2017.
- [26] M. Grupp, "evo: Python package for the evaluation of odometry and slam." <https://github.com/MichaelGrupp/evo>, 2017.